International Journal of Microwave and Wireless Technologies

cambridge.org/mrf

Advanced beam reconfiguration in waveguide antennas through origami inspired design

Chia-Chan Chang[1,2,3], Chia-Chen Lin[1], Meng-Hsuan Lin[1], Sheng-Min Lin[1] and Deng-Chuan Cai[3]

[1]Dept. of Electrical Engineering, National Chung-Cheng University, Chiayi, Taiwan; [2]Advanced Institute of Manufacturing with High-tech Innovations (AIM-HI), National Chung-Cheng University, Chiayi, Taiwan and [3]Graduate School of Design, National Yunlin University of Science and Technology, Yunlin, Taiwan

Research Paper

Cite this article: Chang C-C, Lin C-C, Lin M-H, Lin S-M, Cai D-C (2026) Advanced beam reconfiguration in waveguide antennas through origami inspired design. *International Journal of Microwave and Wireless Technologies* **18**(3), 419–432. https://doi.org/10.1017/S1759078725102821

Received: 2 October 2025
Revised: 11 December 2025
Accepted: 17 December 2025
First published online: 7 January 2026

Keywords
horn antenna; origami; reconfigurable; waveguide

Corresponding author: Chia-Chan Chang; Email: ccchang@ee.ccu.edu.tw

Abstract

This paper proposes and experimentally validates four origami-inspired reconfigurable waveguide antenna designs, including the vertical folded waveguide antenna, the tilted waveguide antenna, the bellowed tilted waveguide antenna, and the fan-fold horn antenna. Aimed at overcoming the inherent limitations of rigid waveguide, those designs use mechanical deformation to control electromagnetic performance. By leveraging simple folding mechanisms, those proposed structures can turn antenna's key parameters such as operating frequency, beam direction, beamwidth, gain and beam shape without relying on active components or complex beamforming circuitry. All prototypes were handcrafted as proof-of-concepts and successfully demonstrated their targeted functionality, showing the great potential in applications that require occasional reconfiguration rather than rapid, continuous adjustment. These results also reveal how origami techniques can unlock new design freedom for compact, reconfigurable antennas for future communication and sensing system.

Introduction

Reliable and efficient signal transmission is extremely essential in wireless communication and sensing systems, where antennas play very crucial role. The continuous evolution of these technologies has driven a demand for antennas that are not only compact and multifunctional but also exhibit high directivity and agile beam control. Conventional antenna designs often struggle to meet these requirements without significant compromises. For instance, achieving high gain typically necessitates large apertures, dense arrays, or specialized structures like lenses and reflectors, while advanced capabilities such as beam steering and beam shaping usually depend on phased array configurations and associated beamforming circuitries. These additions increase hardware complexity, calibration burden, and cost, presenting a great challenge to integrating those features into practical solutions.

For wireless communication systems that do not require rapid adjustments, attention has increasingly shifted toward mechanically reconfigurable antenna structures. In particular, the unique deformability of origami/kirigami-inspired designs has led to growing research on such innovative antenna designs in recent years. The ancient art of origami has inspired a new avenue in engineering. Its core principles, which allow a flat sheet to transform into complex three-dimensional forms, have been successfully adapted to a wide range of applications, from architectures, soft robots, medical devices to space missions (ex. deployable solar panels). This design philosophy has also proven particularly valuable in microwave engineering, providing a new degree of freedom for developing reconfigurable antennas. The literature is now rich with examples of origami/kirigami-inspired antennas. Researchers have extensively utilized these folding and cutting techniques to manipulate key performance metrics, including operating frequency, radiation pattern, and beam direction.

For instance, mechanical actuation through compression has been employed to achieve frequency reconfigurability in helical antennas derived from origami spring architectures [1]. Similarly, complex three-dimensional arrangements, such as Yagi-Uda arrays formed from DNA double helix structures, allow for systematic alteration of the radiation pattern by adjusting the height of individual helix elements [2]. A two-arm Nojima origami conical spiral antenna has been introduced in [3], using the Nojima wrap pattern to morph from a planar dipole into a conical spiral. Other collapsible designs, such as spring-based cube Yagi antennas, enable the modification of the array's effective element count by physically expanding or contracting the cubic structure [4]. A spatial-mapping origami antenna has been developed for CubeSat applications [5], where it produces monopole-like linearly polarized radiation in planar mode but broadside, nearly circularly polarized radiation in folded mode. Furthermore, the rigid origami flasher has been implemented to create robust, thick antennas capable of transformation from

© The Author(s), 2026. Published by Cambridge University Press in association with The European Microwave Association.

a simple dipole to a segmented conical spiral [6]. In parallel, mechanisms relying on discrete movements, like pop-up elements, have proven effective for achieving precise beam steering capabilities [7]. Origami structure sometimes is applied to the antenna carrier instead of antenna itself. For example [8], proposed a deployable broadband millimeter-wave metasurface lens antenna, where the accordion-shaped origami supporter between the source and the lens can be folded/unfolded to switch the operating mode. Another example is the origami-inspired reflectarray antenna [9], which can produce 28 dBi gain, while its deployable structure yields a fourfold increase in aperture area and 92% packing efficiency.

While the application of origami concept to various antenna types has been well-documented, its use in the design of horn antennas remains less explored [10]. Horn antennas have long been a fundamental component of microwave and millimeter-wave systems due to their simple structure, high gain, high efficiency, broad bandwidth, and well-characterized radiation properties. However, a major limitation is their fixed radiation properties once fabricated. Although [10] proposed origami pyramid-like horn antenna for satellite communications, it mainly focused on its foldable volume to provide compactness and adaptability instead of radiation characteristics. Prior research has attempted to overcome this by integrating external structures, such as metasurface lenses to enhance gain and reduce sidelobes [11], or by using a sliding metasurface for mechanical beam steering [12]. These solutions, while effective, often introduce additional material complexity and can be challenging to implement.

Based on the above requirements, this work aims to comprehensively investigate the application of origami techniques to waveguide antennas. An earlier version of this paper was presented at EuCAP 2025 and was published in its Proceedings [13]. In this paper, three more distinct structures employing different folding strategies are further introduced, each enabling mechanical reconfiguration. By folding and compressing the antenna volume, its reconfigurability can be significantly enhanced. The mechanical deformation can directly tune their either operating frequency, beam direction, beamwidth, gain or beam shape in ways that conventional rigid waveguide antennas cannot.

Although the folding strategies differ across designs, the overall approach follows an application-driven workflow: (1) define the deformation required to realize the desired tunable electromagnetic behavior; (2) determine the structural parameters that govern this deformation; and (3) choose a folding pattern capable of producing the intended mechanical transformation. This process enables each folding mechanism to be adapted effectively to its target antenna function.

For consistency, a rectangular waveguide with the length of $L = 187.5$ mm and the transverse dimensions of $a = 100$ mm and $b = 50$ mm is chosen as the reference. This reference configuration serves as the baseline from which various origami-deformed waveguide structures are subsequently derived. The cutoff frequencies of the excited modes can be calculated using (1):

$$f_{c_{mn}} = \frac{c}{2\pi}\sqrt{\left(\frac{m\pi}{a}\right)^2 + \left(\frac{n\pi}{b}\right)^2}, \tag{1}$$

where c is the speed of light, and m, n denote the mode indices.

Accordingly, the fundamental TE_{10} mode of the reference waveguide has a cutoff frequency of 1.5 GHz, while the second modes, TE_{20} and TE_{01}, both have cutoff frequencies of 3.0 GHz. A given TE_{mn} (or TM_{mn}) mode will propagate only if the operating frequency is higher than its corresponded cutoff frequency f_c.

To demonstrate the proof of concept, the proposed antenna prototypes were manufactured by handcraft, therefore unavoidably limits precision and may introduce additional losses. The antennas were built by FR4 printed circuit boards with copper thickness of 0.0275 mm, where 0.8-mm-thick panels are used for the feeding structure and 0.4-mm-thick sheets for those parts requiring extensive folding. After determining the folding geometry, the required mountain–valley crease patterns were generated, transferred onto the FR4 sheets, cut to shape, and folded along the designated crease lines. Each structural joint was then sealed with copper foil tape, not only providing mechanical flexibility but also preventing electromagnetic power leakage. Finally, an SMA connector was inserted from the top, with the probe placed 1/4 guided wavelength away from the waveguide termination.

Vertical folded waveguide antenna

This section first introduces a vertically folded waveguide antenna with adjustable internal dimensions. The core mechanism involves using an external force to create structural deformation, thereby achieving a change in its operating frequency and antenna gain.

Theoretical concept

As illustrated in Fig. 1(a), the design incorporates foldable side walls, which are bent and folded into deformable upper and lower sections. The sidewall's fold line is located at the midpoint of dimension b, so the upper and lower sections are equal in size and tilt symmetrically about the fold line, thereby enabling the vertical folding mechanism. Note that the fold line can be either a mountain fold or a valley fold, allowing the waveguide to expand outward or contract inward.

To investigate the influence of the deformed structure on the waveguide's performance, this study defines the folded angle θ as the inward bending angle of the waveguide's inner walls. During the deformation, different folded angles result in varying waveguide cavity sizes, leading to the change of the operating frequency. The electromagnetic (EM) simulations in Ansys HFSS (High Frequency Structure Simulator) were performed for folded angles ranging from 60° to 120° in 10° increments. The simulation results, shown in Fig. 1(b), demonstrate that as the folded angle increases, the cutoff frequency of the fundamental TE_{10} mode in the waveguide gradually shifts toward lower frequencies.

From a structural perspective, the dimension a (the distance between the side walls) changes with the folded angle and thereby influences the cutoff frequency. Although dimension b changes as well, it has little effect on the TE_{10} mode according to (2). Further analysis reveals that the effective broad dimension of a is equivalent to the average distance between the inclined sidewalls, denoted here as a_{avg}, can be defined as (3). In this case, the fold line is located at midpoint of b so that the effective broad dimension is $a_{avg} = a[1\text{-}(b/2)\cos\theta]$:

$$f_{c_TE_{10}} = \frac{c}{2a}, \tag{2}$$

$$a_{avg} = \left(\frac{1}{n}\right)\sum_{i=1}^{n} a_i. \tag{3}$$

As shown in Fig. 2, the calculated cutoff frequencies based on a_{avg} exhibit good agreement with the simulation results. This observation indicates that the cutoff frequency of a vertically folded waveguide can be effectively tuned through structural

https://doi.org/10.1017/S1759078725102821 Published online by Cambridge University Press

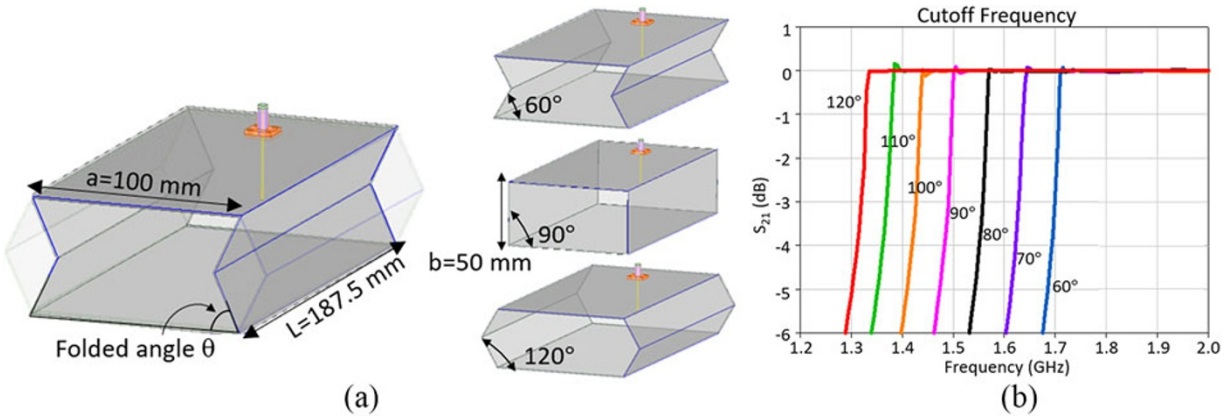


Figure 1. (a) Proposed vertical folded waveguide, (b) Simulated cutoff frequencies for various folded angles.

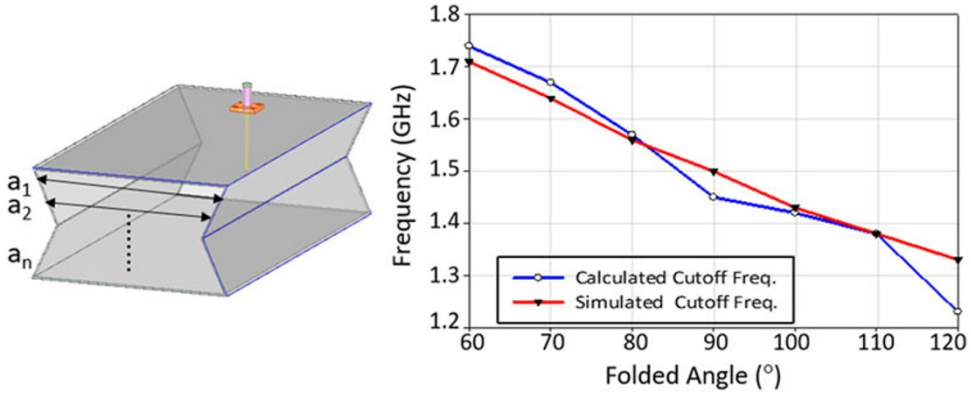


Figure 2. Comparison of the simulated and calculated TE_{10} cutoff frequency.

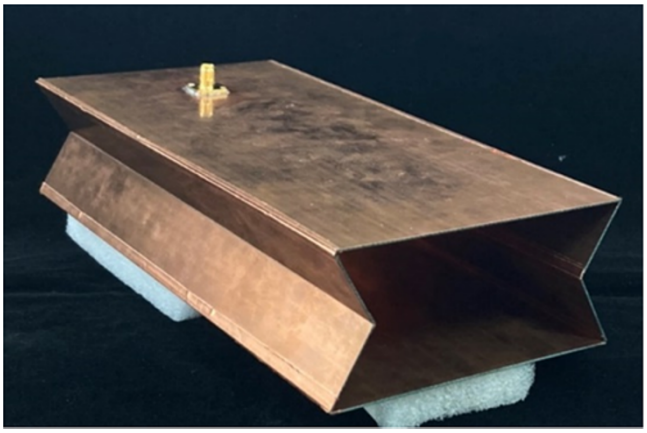


Figure 3. Fabricated prototype of the vertically folded waveguide.

deformation. Such tunability offers significant advantages for the design of multiband antenna systems.

The fabricated prototype is shown in Fig. 3. Each sidewall was realized by assembling two separate FR4 panels, which were mechanically joined and electrically connected using copper foil tape. This configuration allows the sidewalls to be foldable, thereby enabling the intended structural deformation.

Simulations and measurements

This vertically folded waveguide was treated as an open-ended waveguide antenna for performance evaluation. Figure 4 shows both simulated and measured return loss (S_{11}) at three folded angles (60°, 90°, and 120°). The simulation shows that the corresponding resonant frequencies are 2.81 GHz (60°), 2.74 GHz (90°), and 2.66 GHz (120°). As the folded angle increases, the effective cavity dimension expands, resulting in a downward shift of approximately 150 MHz in the resonant frequency. The measured results, 2.80 GHz (60°), 2.74 GHz (90°), and 2.66 GHz (120°), exhibit excellent agreement with the simulations.

Figure 5 presents both simulated and measured radiation patterns of this open-ended waveguide antenna at 2.75 GHz. It can be observed that the radiation characteristics in the *XZ*-plane (*H*-plane) exhibit obvious variations as the folded angle increases. When the folded angle θ changes from 60° to 120°, the main beam in the *H*-plane gradually becomes narrower, accompanied by an improvement in directivity. Correspondingly, the antenna gain increases slightly from 6.8 to 7.9 dBi, while the half-power beamwidth is reduced from 66° to 52°. In contrast, the radiation patterns in the *YZ*-plane (*E*-plane) remain relatively stable with less significant variation.

The measured results reveal a similar trend. Due to the handcrafted nature of the prototype, the measured gain was slightly lower than expected. Specifically, the main-lobe gain in the *H*-plane was approximately 4.8 dBi at $\theta = 60°$, increasing to about 7 dBi at $\theta = 120°$ as the beam gradually narrowed with larger folded

https://doi.org/10.1017/S1759078725102821 Published online by Cambridge University Press

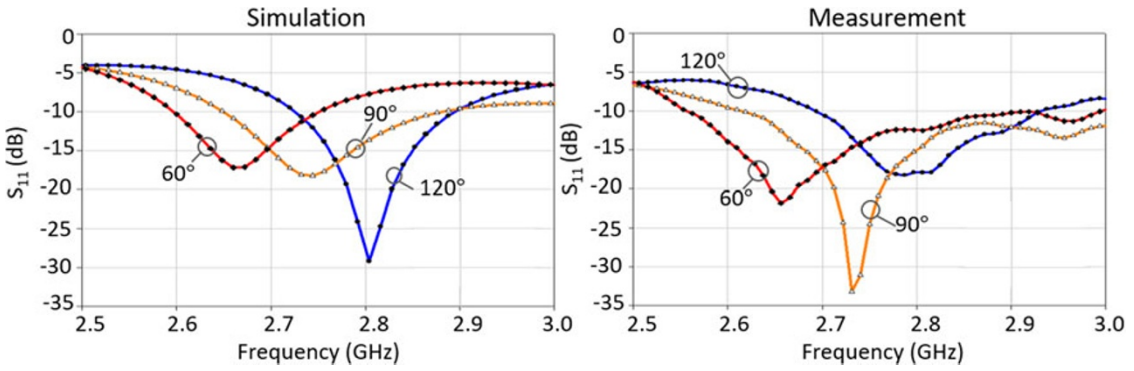


Figure 4. Return loss with different folded angles.

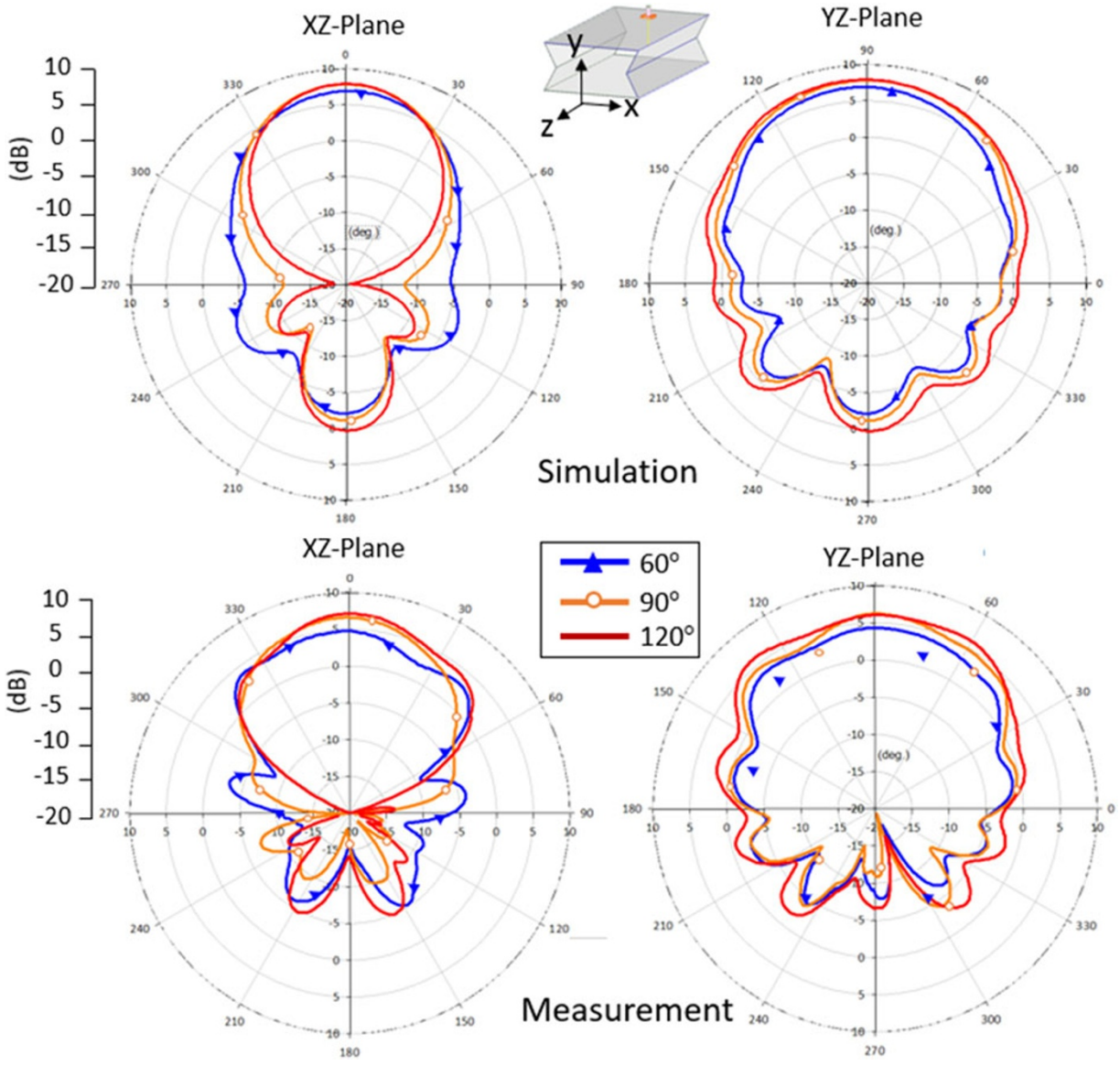


Figure 5. Radiation patterns of the vertically folded waveguide antenna.

angles. This behavior can be attributed to the structural changes induced by sidewall folding. The effective broad dimension a_{avg} varies significantly, from 75 mm at 60° to 125 mm at 120°, while the narrow dimension b undergoes only a minor change, ranging from 43 mm (60°, 120°) to 50 mm (90°). Consequently, the radiation patterns exhibit more obvious variations in the H-plane compared

https://doi.org/10.1017/S1759078725102821 Published online by Cambridge University Press

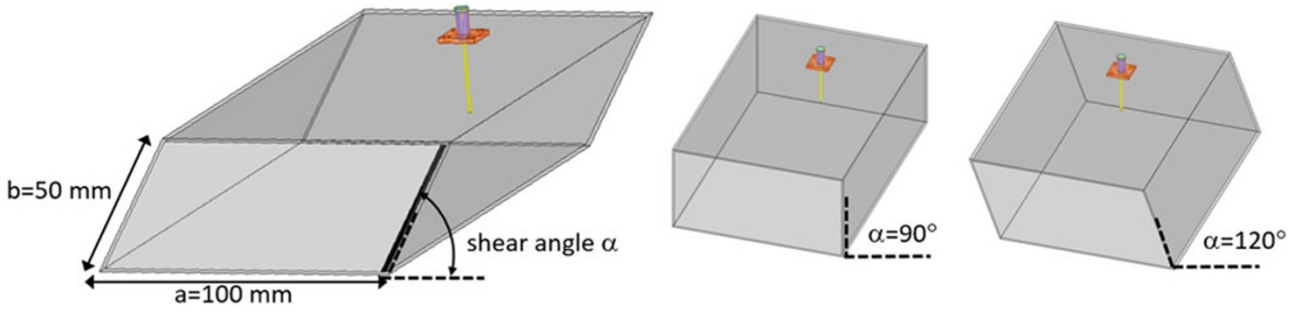


Figure 6. Proposed tilted waveguide.

with the *E*-plane. Furthermore, the larger effective aperture at a 120° folded angle accounts for the observed enhancement in antenna gain.

In brief summary, the proposed vertically folded waveguide antenna demonstrates that structural folding is an effective approach to control the aperture dimension, enable beam shaping as well as gain adjusting.

Tilted waveguide antenna

This section introduces a tilted waveguide structure with an obliquely tilted cross-section. The main concept is to exploit its non-orthogonal geometry to manipulate the internal field distribution, enabling changes in beam direction through controlled structural deformation.

Theoretical concept

Unlike the conventional rectangular waveguides have orthogonal boundaries, this proposed design maintains a constant separation between the parallel broad walls, while the waveguide's lateral sidewalls are tilted with respect to the propagation axis. This geometric manipulation creates an inherently asymmetric cavity, resulting in a parallelogrammatic cross-section. The sidewall's tilt angle, which is defined as shear angle α, is the angle between the tilted lateral sidewall and the waveguide's broad plane, as shown in Fig. 6.

The tilted structure forces the energy distribution within the cavity to become non-uniform and asymmetrical. When the geometry of the waveguide departs from orthogonal symmetry, as in this case, higher-order modes can interact in non-trivial ways.

Above cutoff, the mode propagates with propagation constant β_{mn}:

$$\beta_{mn} = \sqrt{k_0{}^2 - \left(\frac{m\pi}{a}\right)^2 - \left(\frac{n\pi}{b}\right)^2}, \quad (4)$$

where $k_0 = 2\pi f$ /c is the free-space wavenumber.

When multiple propagating modes coexist, the total field is a superposition, as shown in (5). Since different modes propagate with different β values, the interference of these terms creates a composite field distribution with relative phase differences $\Delta\phi z = (\beta_1 - \beta_2)z$:

$$E(x,y,z) = A_1 E_1(x,y)\, e^{-j\beta_1 z} + A_2 E_2(x,y)\, e^{-j\beta_2 z}. \quad (5)$$

If the aperture is tilted, the boundary conditions project the superimposed fields onto different directions in space, effectively coupling modal interference to radiated beam steering. The radiation beam direction θ can be approximated by a phase-matching condition $k_0 \sin\theta \approx ((\beta_1 - \beta_2)$. Thus, the beam tilt is not a consequence of frequency alone, but of multi-mode interference in a tilted boundary geometry.

Figure 7 simulated electric-field distributions and radiation patterns of the 60°-tilted waveguide antenna at different operating frequencies. At 2.0 GHz, only the fundamental mode propagates in the waveguide, producing a symmetric field and a purely longitudinal propagation constant. Consequently, the radiated beam aligns with the aperture normal without noticeable steering. At 3.3 GHz, the operating frequency exceeds the second-mode cutoff (3 GHz). The combined effect of internal reflections and dual-mode interactions produces an asymmetric aperture field, which in turn leads to the observed beam steering at the waveguide opening. At 3.8 GHz, multiple higher-order modes are excited. The aperture field thus becomes a superposition of three or more modes, resulting in a much more complex distribution. The accumulated phase differences increase rapidly at higher frequencies, producing a multi-peaked phase front at the opening and leading to beam-splitting phenomena.

Because different modal components coexist and interfere, causing the field to bounce between the inclined walls, the length of the tilted waveguide directly influences the radiation pattern at the opening since the wave progresses along the structure. Figure 8 shows the simulated electric-field distributions for a 60°-tilted waveguide with different waveguide lengths. It can be observed that the waveguide length determines the direction of the radiated beam at the opening. Figure 8 also compares the far-field radiation patterns for $L = 187.5$ mm (1.25 λg) and $L = 337$ mm (2.25 λg), revealing that the beam directions in *H*-plane are almost reversed between those two cases. These results confirm that, in addition to the shear angle, the waveguide length plays a critical role in determining the beam-steering angle of the tilted waveguide antenna. To align the structure's inclination with the beam steering direction for more intuitive operation, $L = 187.5$ mm was selected in this work.

Figure 9 shows the fabricated prototypes. To enhance the radiation performance, two metallic plates were added to the aperture of the tilted waveguide, forming a flared extension. These tapered plates act as a gradual transition from the waveguide to free space, increasing the effective aperture area. The flared angle and flared length are 30° and 60 mm, respectively.

Simulations and measurements

Figure 10 presents the simulated and measured return loss (S_{11}) of the proposed tilted waveguide antenna at 3.3 GHz. In the simulations, all angle pairs, including 60°/120°, 70°/110°, and 80°/100°, exhibit nearly identical S_{11} responses. This similarity arises from

https://doi.org/10.1017/S1759078725102821 Published online by Cambridge University Press

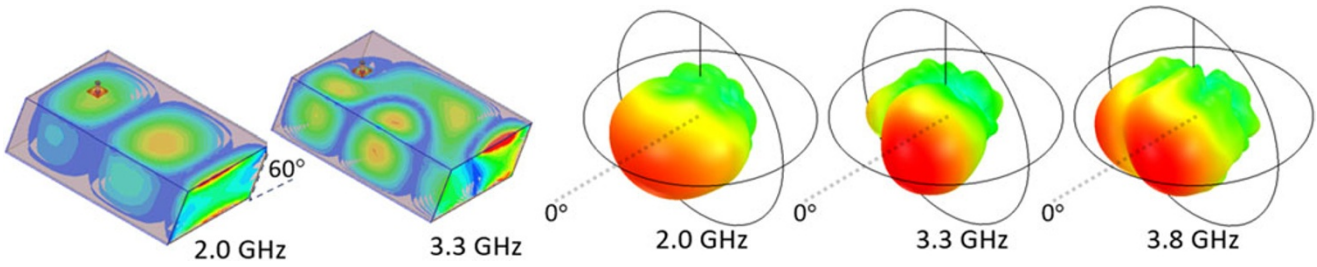


Figure 7. *E*-field distributions (left) and radiation patterns (right) of the tilted waveguide antenna.

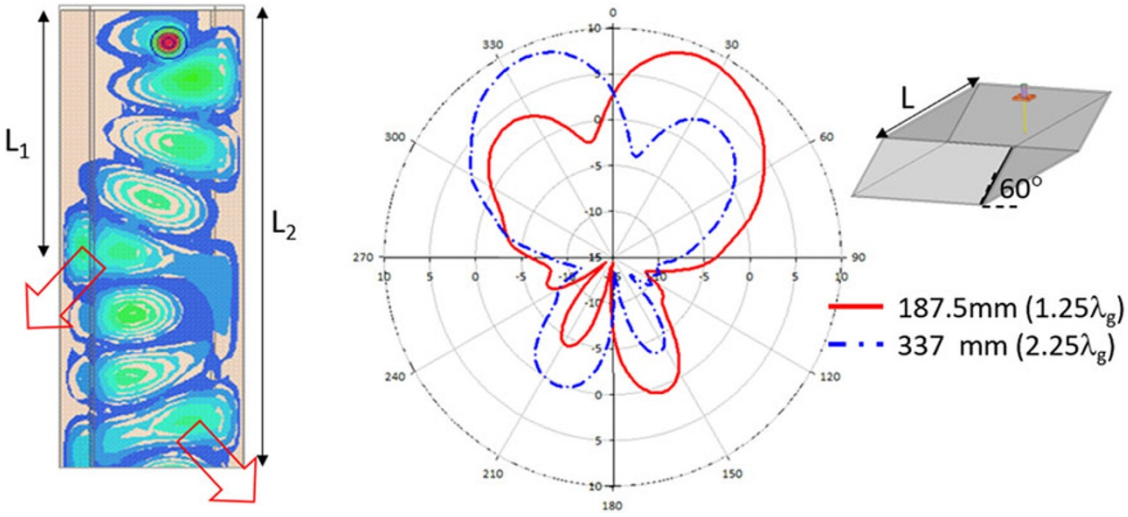


Figure 8. Electric-field distributions and radiation patterns with different waveguide length.

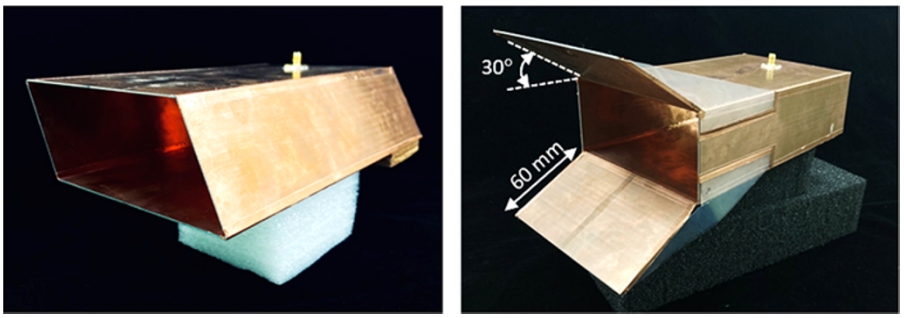


Figure 9. Fabricated prototypes of the tilted waveguide without (left) and with (right) flared extension.

the intrinsic structural symmetry of the waveguide. For each paired configuration, the internal cavity geometry is effectively mirrored across the central axis, resulting in symmetrical electromagnetic characteristics. The measured results for these symmetric angle pairs show only minor deviations, attributable to fabrication tolerances and experimental inaccuracies. Nevertheless, the overall measurement trends agree well with the simulations.

The simulated and measured *XZ*-plane (*H*-plane) radiation patterns are shown in Fig. 11. In simulation, the peak gain remains relatively stable between 10.3 and 11.5 dBi across all shear angles, while the main beam steering gradually shifts from +23° at $\alpha = 60°$ to (−22)° at $\alpha = 120°$. The measurements show a similar trend, with peak gains ranging from 8.5 to 11.5 dBi and beam steering moving from +28° at $\alpha = 60°$ shear to (−28)° at $\alpha = 120°$. Because the shear angles were adjusted manually, minor deviations from the intended shear angles may lead to modest differences in the beam-steering direction between simulation and measurement. Nevertheless, the trends of peak gain, beam-steering angle, and the half-power beamwidth (HPBW) show strong agreement between the simulated and measured results, confirming the validity of the proposed design concept. The simulated and measured performance of the proposed tilted waveguide antenna are summarized in Table 1.

Since single-mode operation is usually desired, the primary concern with the proposed tilted waveguide operating in dual modes is modal dispersion. When two or more modes propagate simultaneously, they exhibit different propagation constants and group velocities, inevitably leading to differential modal delay. For narrowband single-tone or low modulation-depth signals, this effect may be negligible. However, for broadband or high data rate signals, it can cause phase/amplitude distortion and thus degrade signal integrity. To examine this practical issue, a communication

https://doi.org/10.1017/S1759078725102821 Published online by Cambridge University Press

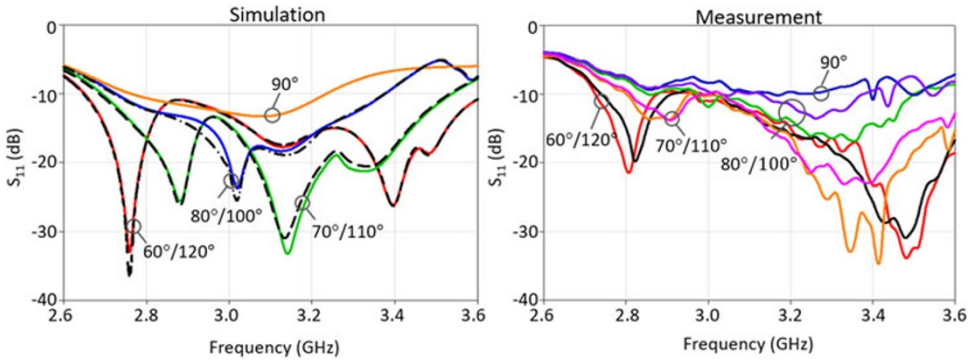


Figure 10. Return loss with different shear angles.

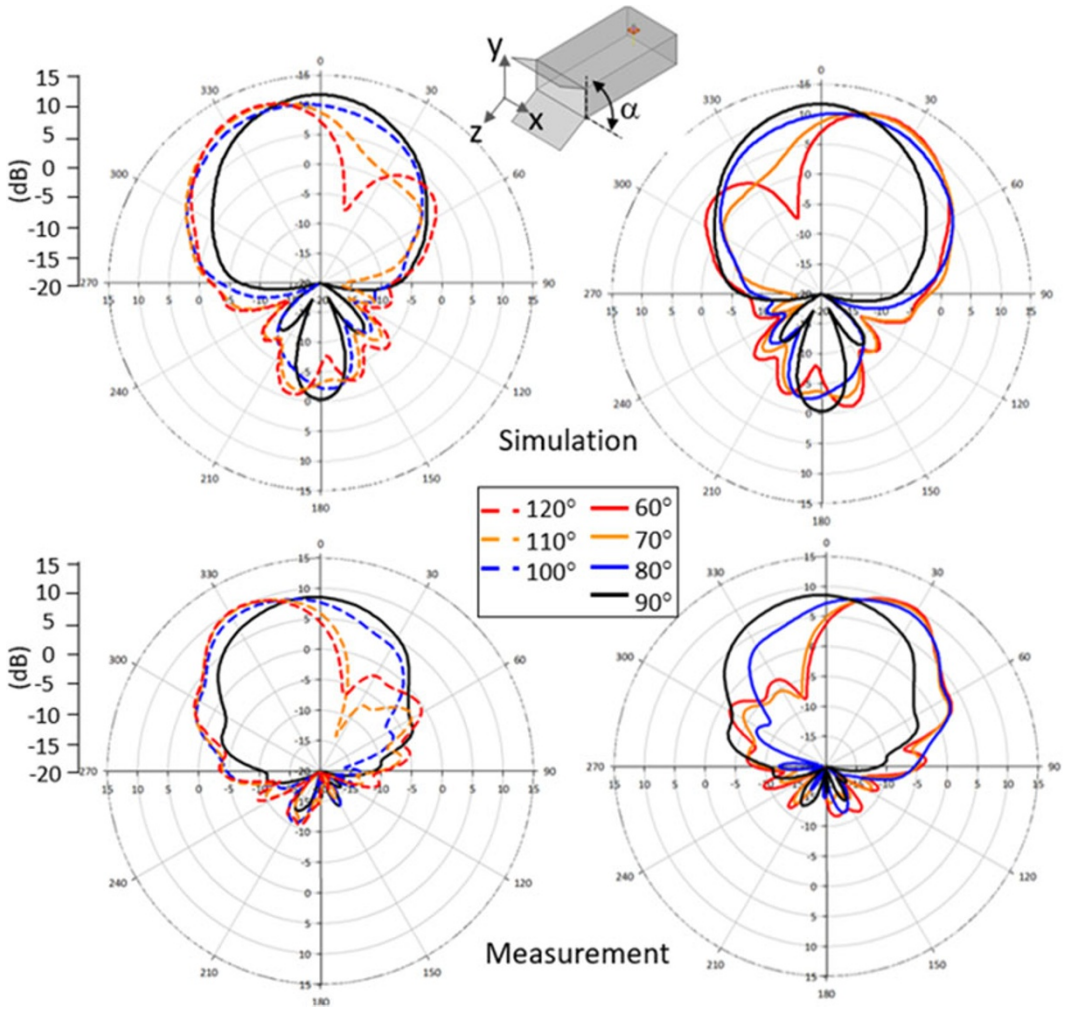


Figure 11. Radiation patterns (*XZ*-plane) of the tilted waveguide antenna.

experiment using a realistically modulated 64-QAM (quadrature amplitude modulation) signal was performed. Furthermore, in the measurement setup, a misalignment was intentionally introduced between the transmitting and receiving antennas, while the tilted waveguide antenna can demonstrate its beam-steering capability to capture signals arriving from off-axis directions. The results indicate that, within the beam-steering range of ±28°, the measured error vector magnitude (EVM) stays below 3.5%, demonstrating that good signal quality is maintained over the tested steering angles despite multi-mode propagation.

Bellowed tilted waveguide antenna

As noted above, the tilted waveguide is sensitive to its length. To increase the degree of tunability, an origami-inspired bellow

https://doi.org/10.1017/S1759078725102821 Published online by Cambridge University Press

Table 1. Performance comparison of the tilted waveguide antenna

	Simulation			Measurement		
Shear angle α	Peak gain (dBi)	Beam steering	HPBW	Peak gain (dBi)	Beam steering	HPBW
60°	11.5	23°	42.1°	10.1	28°	33.4°
70°	11.2	20°	48.1°	9.7	26°	36.7°
80°	10.3	14°	74.2°	9.1	23°	51.6°
90°	11.6	0°	53.4°	8.5	−2°	65.7°
100°	10.3	−14°	74.2°	9.1	−22°	55.2°
110°	11.2	−20°	49.9°	9.8	−27°	41.9°
120°	11.5	−22°	41.3°	11.5	−28°	36.2°

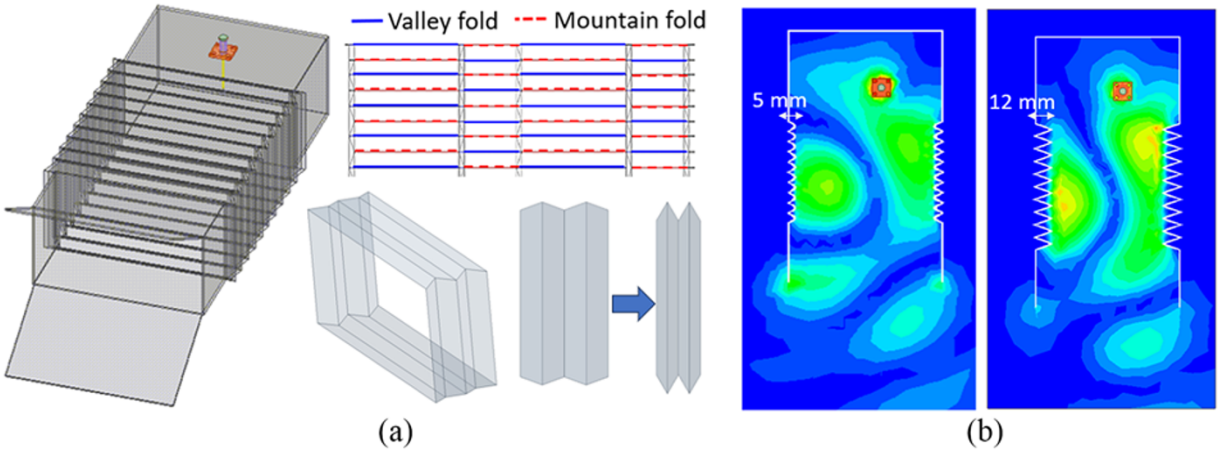


Figure 12. (a) Bellowed tilted waveguide with fold patterns and (b) *E*-field distributions with different corrugation depths.

structure is incorporated into the design to allow fine adjustment of the waveguide length, as shown in Fig. 12(a). However, tuning the bellowed section alone does not provide smooth or continuous beam steering. As seen in Fig. 8, changing only the length causes the main beam to jump between a few extreme angles rather than producing evenly spaced or wide-angle scanning. Thus, length tuning is better suited for discrete beam switching or minor performance adjustments, while the shear angle remains the primary and more reliable parameter for achieving controllable and well-distributed beam steering across the angular range.

The bellowed waveguide produces non-smooth sidewalls that alter the original boundary conditions. To evaluate its impact, electric-field distributions were simulated for corrugation depths of 5 and 12 mm, as seen in Fig. 12(b). Results show that a smaller corrugation depth yields a smoother structure, while 12-mm corrugation chaotic energy distribution due to highly irregular sidewalls. Taking both waveguide performance and folding difficulty into account, a corrugation depth of 5 mm was selected in this work. Simulation results also show that, for the same length and the same shear angle, the radiation patterns of structures with and without corrugation exhibit very close agreement, as seen in Fig. 13. This further confirms that the corrugation has negligible impact.

Figure 14 illustrates the implementation of the proposed bellowed tilted waveguide antenna. Because the bellowed structure is more complex, a crease layout with mountain and valley fold lines was first generated using drawing software. This layout was then printed at a 1:1 scale onto transparent adhesive film, placed over the FR4 sheet, and used as a guide to cut the crease lines before folding. The bellowed section uses 0.4-mm-thick FR4 for easier folding, while the remaining parts use 0.8-mm-thick substrate.

While the material thickness limits the bellowed section's deformation, the achievable range from 131 to 206 mm is adequate for optimization. By tuning the structure, the length was reduced to $L = 169$ mm, resulting in improved performance. As illustrated in Fig. 15 and Table 2, the bellowed version, compared with the previous tilted waveguide antenna without the bellowed section, achieves a slightly smaller steering range of ±25° but retains a higher and more stable peak gain (gain variation <1 dB). In addition, the beam directions at different shear angles are more evenly distributed in space, significantly enhancing its practical applicability. Note that the slight differences in performance arise from the small discrepancy in physical length between the two structures. Nevertheless, the overall performance trends and tuning capabilities remain consistent.

Fan-fold horn antenna

The radiation property of horn antennas is fundamentally determined by their aperture dimensions. Conventional horn is rigid, with parameters such as flare length and flare angle being fixed. In this section, we propose an alternative concept that employs an origami-inspired horn antenna with a fan-fold aperture [10]. The aperture geometry can be mechanically reconfigured to dynamically adjust the beam shape, gain, and direction.

https://doi.org/10.1017/S1759078725102821 Published online by Cambridge University Press

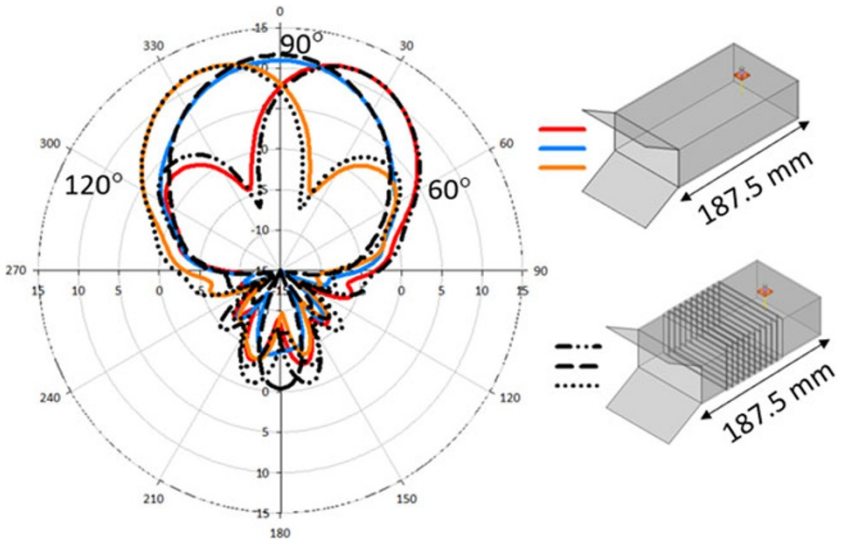


Figure 13. Radiation patterns with and without corrugation.

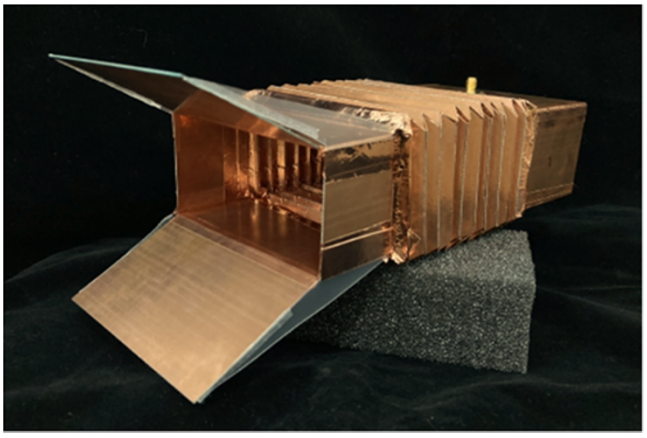


Figure 14. Fabricated prototypes of the bellowed tilted waveguide antenna.

Theoretical concept

To implement this concept, an H-plane sectoral horn configuration was adopted in this work. This arrangement expands the waveguide solely in the H-plane while preserving the E-plane dimension, producing a highly directional, fan-shaped beam whose width can be tailored in the H-plane while remaining nearly constant in the E-plane, as shown in Fig. 15. Closed-form expressions for the directivity of an H-plane sectoral horn are given in (6)–(8). In these formulas a and b denote the cross-sectional dimensions of the feeding waveguide, a_1 is the aperture dimension along the wider side of the horn opening, and ρ_2 denotes the flare length that is the distance from the point where the guide begins to expand to the edge of the aperture in the H-plane. The Fresnel integrals C(u), C(v), S(u), and S(v) appear in these expressions to account for the aperture phase distribution:

$$D_H = \frac{4\pi b\rho_2}{\lambda a_1}\left\{\left[C(u)-C(\nu)\right]^2+\left[S(u)-S(\nu)\right]^2\right\}, \quad (6)$$

$$u = \frac{1}{\sqrt{2}}\left(\frac{\sqrt{\lambda\rho_2}}{a_1}+\frac{a_1}{\sqrt{\lambda\rho_2}}\right), \quad (7)$$

$$\nu = \frac{1}{\sqrt{2}}\left(\frac{\sqrt{\lambda\rho_2}}{a_1}-\frac{a_1}{\sqrt{\lambda\rho_2}}\right). \quad (8)$$

Figure 16 also shows the horn aperture constructed with a fan-fold origami structure together with its detailed dimensions. In this configuration, alternating mountain and valley folds are arranged in an interleaved pattern, allowing the controlled expansion and contraction of the horn walls. The fold geometry provides a compliant mechanism that enables real-time adjustment of the aperture while preserving the intended shape. Each fan blade measures 150 mm in length with 8.6 mm spacing between adjacent blades, and the two opposing sets of blades are positioned 10 cm apart. With the flare length held constant, this folding mechanism enables mechanical adjustment of the flare angle θ to tune the antenna aperture while simultaneously preserving mechanical stability during operation.

To further evaluate the influence of the folded geometry on the field distribution, Fig. 17 compares the top- and cross-sectional views of the E-field in a conventional sectoral horn and fan-fold sectoral horn. The results indicate that the introduction of the folding pattern only cause a minimal perturbation of the field distribution. This behavior arises because the E-field of the dominant TE_{10} mode inherently exhibits a cosine-like variation across the aperture width, with the maximum field intensity at the center gradually tapering toward the edges.

Figure 18 presents the implemented prototype. The feeding waveguide section is fabricated from a 0.8-mm-thick FR4 substrate, whereas the fan-shaped aperture is constructed using a 0.4-mm-thick FR4 panel. However, due to the finite material thickness, the fan blades cannot be fully folded. Even in the most compact configuration, the flare angle still remains at least 10°.

Simulations and measurements

With independent actuation of each side, this structure enables two operating modes. For double-sided flaring, in which both sides of the aperture are folded or unfolded simultaneously while maintaining structural symmetry, the goal is to achieve gain tuning or beam shaping. Measurements were conducted with the flare angle beginning at 10° and increased in 5° increments up to 30°.

https://doi.org/10.1017/S1759078725102821 Published online by Cambridge University Press

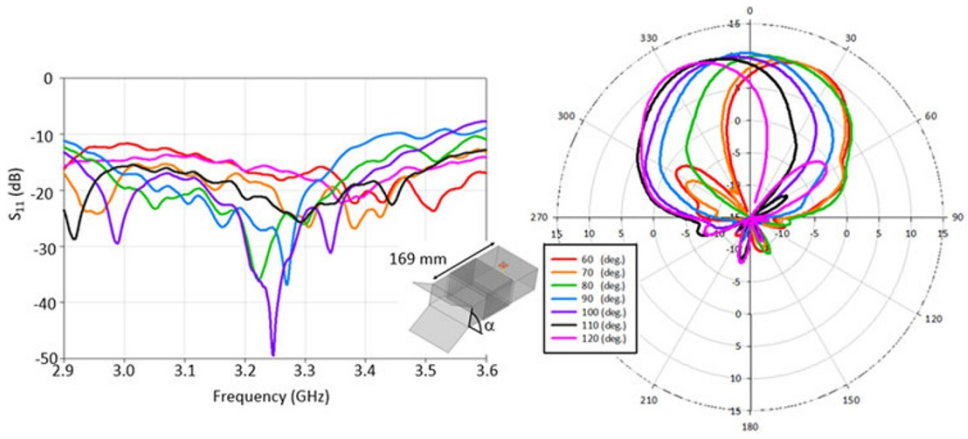


Figure 15. Measured return loss and radiation patterns of the bellowed tilted waveguide antenna.

Table 2. Comparison of bellowed and non-bellowed tilted waveguide antennas

	Bellowed tiled waveguide antenna (L = 169 mm)			Tiled waveguide antenna (L = 187.5 mm)		
Shear Angle	Peak gain (dBi)	Beam Steering	HPBW	Peak gain (dBi)	Beam Steering	HPBW
60°	10	25°	43.4°	10.1	28°	33.4°
70°	10.1	19°	45.2°	9.7	26°	36.7°
80°	10.1	7°	59.9°	9.1	23°	51.6°
90°	10.4	−2°	49.9°	8.5	−2°	65.7°
100°	9.9	−9°	56.9°	9.1	−22°	55.2°
110°	10.1	−16°	55.8°	9.8	−27°	41.9°
120°	10.5	−25°	42.0°	11.5	−28°	36.2°

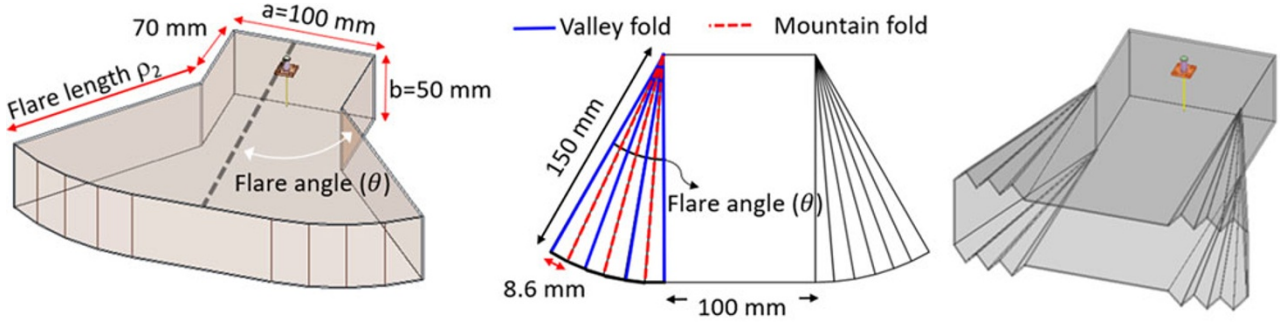


Figure 16. *H*-plane sectoral horn antenna with origami fan-fold aperture.

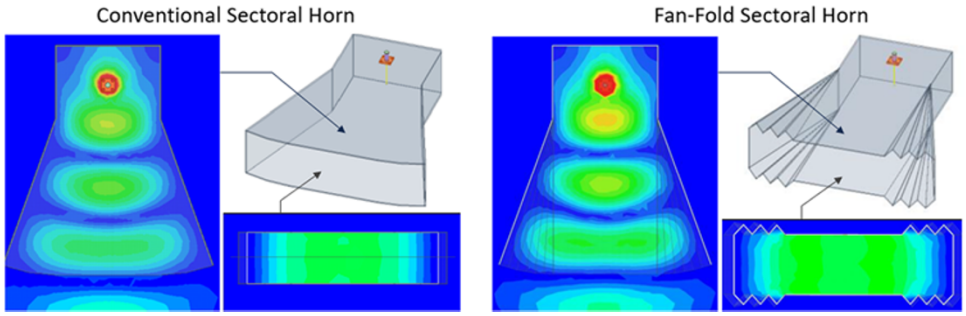


Figure 17. E-field distribution in conventional and fan-fold sectoral horns.

https://doi.org/10.1017/S1759078725102821 Published online by Cambridge University Press

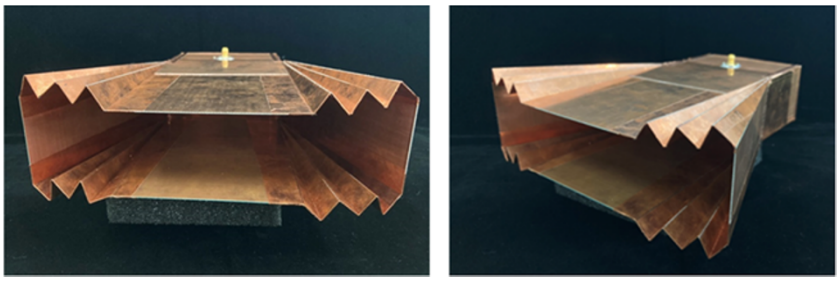


Figure 18. Fabricated fan-fold horn antenna.

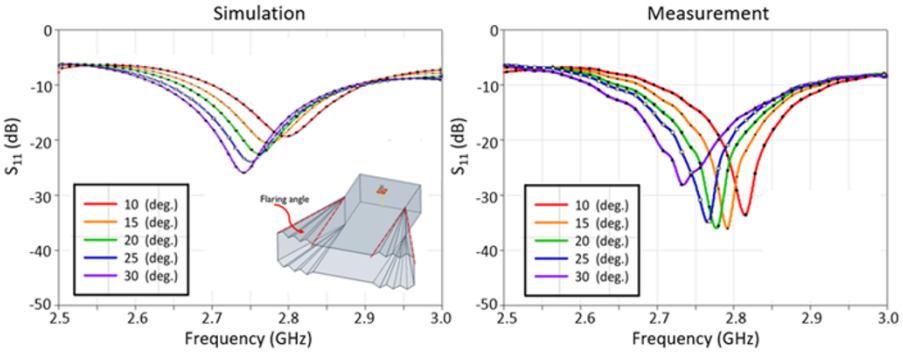


Figure 19. Return loss from double-sided flaring configuration.

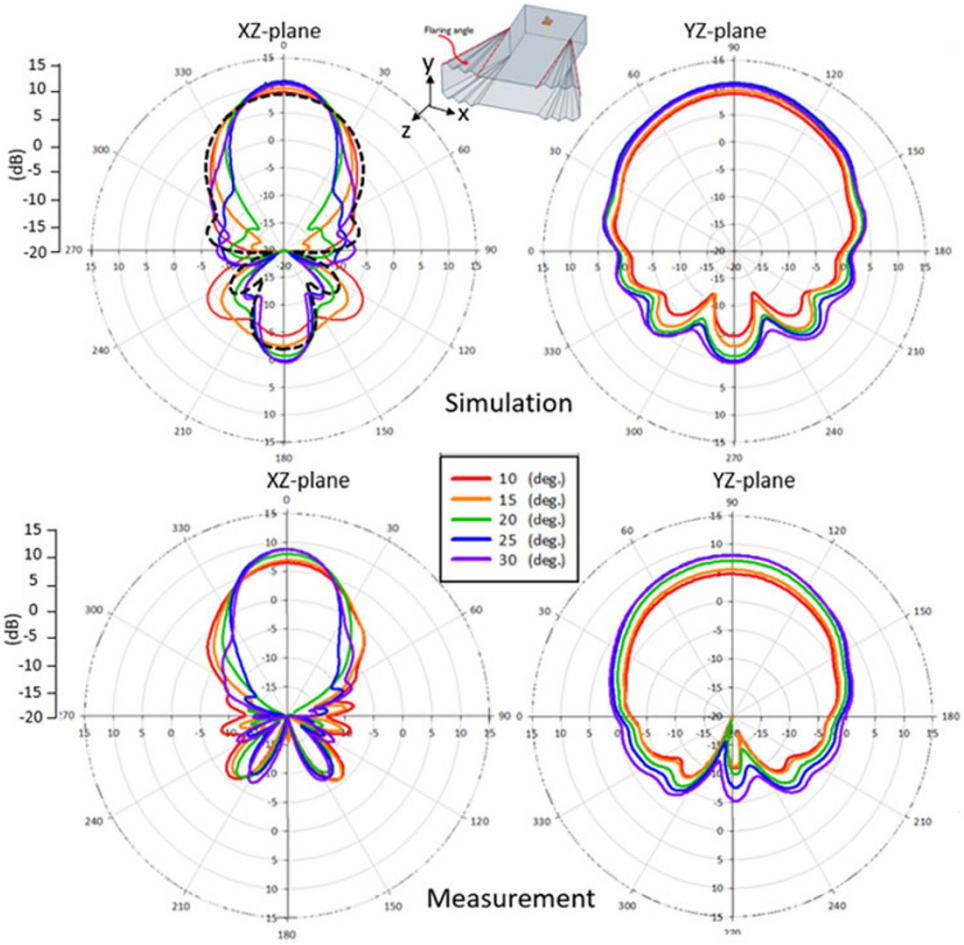


Figure 20. Radiation patterns of the double-sided flaring configuration.

Figure 19 presents the simulated and measured return loss as a function of flare angle. Both shows that the resonant frequency shifts toward lower values with increasing flare angle (simulation: 2.80 GHz at 10° to 2.74 GHz at 30°; measurement: 2.82 GHz at 10°

https://doi.org/10.1017/S1759078725102821 Published online by Cambridge University Press

Table 3. Performance comparison from double-sided flaring configuration

Double-sided flaring case (for gain tuning/beam shaping)				
	Simulation		Measurement	
Flare angle θ	Max. gain (dBi)	HPBW	Max. gain (dBi)	HPBW
10°	8.7	48°	6.4	46.2°
15°	9.4	43.4°	6.9	44.6°
20°	10.4	34.9°	7.4	36.4°
25°	10.7	31.6°	8.7	32.4°
30°	9.5	29.9°	8.7	33.0°

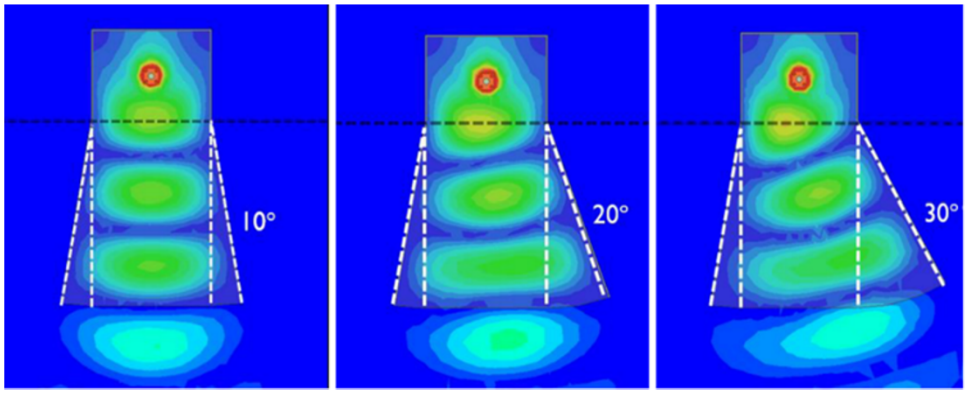


Figure 21. E-field distribution from single-sided flaring configuration.

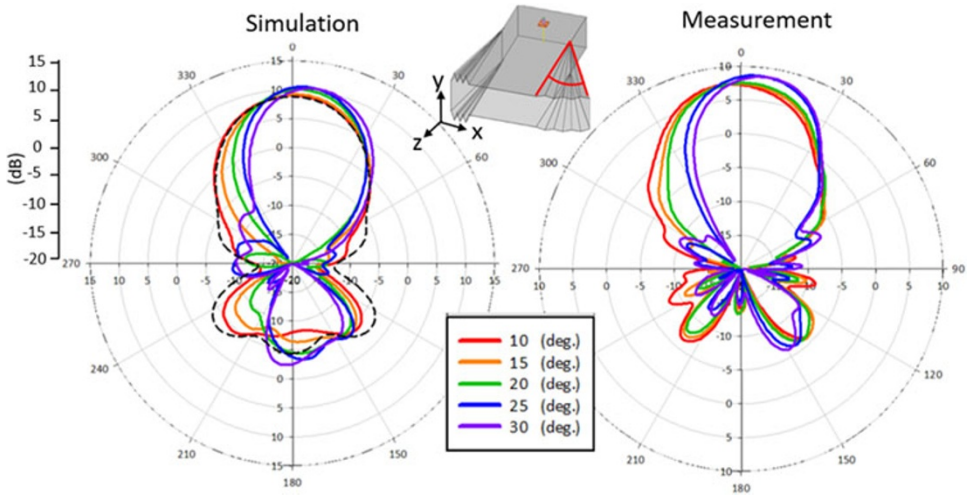


Figure 22. Radiation patterns from single-sided flaring configuration.

to 2.73 GHz at 30°). This behavior reflects the fact that enlarging the aperture also increases the electrical volume of the antenna, thereby lowering its natural resonance.

Figure 20 compares the simulated and measured radiation patterns at 2.7 GHz, showing good agreement between each other. In the *YZ*-plane (*E*-plane), varying the flare angle does not alter the radiation pattern. In contrast, in the *XZ*-plane (*H*-plane), increasing the flare angle enlarges the aperture dimension of that cross section, leading to a corresponding rise in gain. In the simulations, increasing the flare angle from 10° to 30° produces a 2-dB gain enhancement, reaching a maximum of 10.7 dBi, while the 3-dB beamwidth narrows from 48° to 29.9°. The measured results, although 2–3 dB lower due to fabrication tolerances, exhibit the same trend, with a maximum gain of 8.8 dBi and a 3-dB beamwidth narrowing from 46.2° to 33.0°. These results demonstrate that the proposed fan-fold horn antenna can adjust its aperture flare angle through folding actions, thereby effectively tuning its radiation characteristics. Both simulation and measurement data are summarized in Table 3.

In the single-sided flaring configuration, one side of the aperture remains fixed while the opposite side is progressively opened, creating an asymmetric aperture whose operation is aimed at

https://doi.org/10.1017/S1759078725102821 Published online by Cambridge University Press

Table 4. Performance comparison from single-sided flaring configuration

Single-sided flaring case (for beam steering)						
	Simulation			Measurement		
Flare angle θ	Gain (dBi)	HPBW	Steering	Gain (dBi)	HPBW	Steering
10°	8.9	47.3°	0°	6.7	46.3°	−2°
15°	9.1	44.1°	2°	6.9	45.0°	1°
20°	10.0	38.4°	3°	7.0	44.5°	2°
25°	10.5	34.5°	5°	8.1	37.3°	6°
30°	10.3	35.1°	9°	8.0	35.3°	9°

achieving beam steering. In this arrangement, the fan blades on one side are kept tightly folded, whereas those on the other side are unfolded with the flare angle varied from 10° to 30° in 5° increments. Figure 21 shows the corresponding E-field distributions. With both sides set to the initial 10° angle, the antenna geometry remains symmetric and the field distribution is nearly uniform, directing most of the power forward. As the flare angle on one side increases, the aperture becomes progressively asymmetric, causing the electric field to tilt toward the side with the larger flare angle and thereby producing a beam-steering effect.

Figure 22 compares the simulated and measured radiation patterns in the *XZ*-plane, again demonstrating good agreement between those data. As the flare angle is varied, the main beam direction is shifting correspondingly. In the simulations, the maximum steering reaches 10°, while the measurements indicate a maximum of approximately 11°. In addition to the steering effect, the gain also increases as the aperture is enlarged. The current structure restricts the flare angle to 30°, thereby limiting the beam-steering capability to approximately ±10°. Increasing the number of fan blades is expected to further expand the achievable steering range. Both simulation and measurement results are summarized in Table 4.

Conclusion

In this study, four origami-inspired waveguide antennas were introduced and experimentally validated. The demonstrations show that by controlled folding, antennas can be mechanically reconfigured to change their radiation properties without relying on active components or complex external circuitry. Those results highlight the potential of origami techniques to unlock new functionalities in horn antennas, pointing toward advanced, multi-functional systems that are both cost-effective and easy to manufacture. While such mechanical reconfiguration is generally unsuitable for communication environments requiring dynamic and rapid change, it offers a practical and low-complexity solution for applications such as fixed infrastructure or measurement systems, where simple structural adjustments can correct or compensate for long-term environmental drift or preset configuration changes.

Although the proposed concepts were successfully demonstrated, several practical issues remain unresolved. Because all prototypes were handcrafted as proof-of-concepts, higher losses and fabrication tolerances were unavoidable. Moreover, the deformation control lacked sufficient precision, leading to slight discrepancies between simulation and measurement. Therefore, future implementations will require improvements in mechanical accuracy and overall circuit robustness. Incorporating mechanical fixtures to precisely set and maintain the deformation states is also necessary. Furthermore, the 0.4-mm FR4 used for the foldable sections provides sufficient support but limited flexibility, which restricts the achievable deformation. Future designs may use more flexible materials, such as PP synthetic paper laminated with copper foil tape, to enable larger folding motions as well as to improve overall reconfigurability.

Ultimately, this study illustrates how interdisciplinary collaboration, linking traditional folding arts with microwave circuit design, can challenge the inherent limitations of conventional rigid waveguide antennas. By merging origami principles with antenna technology, this approach opens new possibilities for compact, reconfigurable structures capable of meeting the evolving needs of modern communication and sensing systems. Looking ahead, origami-inspired antennas present several promising research directions. While the present work focuses on pure folding mechanisms, incorporating kirigami (cut-based geometries) may further expand the design space and enable mechanical transformations that are difficult to realize through folding alone. The combination of origami and kirigami introduces additional degrees of freedom, such as localized stretching, reconfigurable apertures, and adaptive panel segmentation, potentially leading to multifunctional antenna structures with enhanced beam control or frequency agility. We hope that this work will inspire further innovation and help pave a new design avenue for next-generation circuits.

Acknowledgement. The authors would like to thank Dr. Shih-Cheng Lin, Dr. Janne-Wha Wu, and Dr. Sheng-Fuh Chang for their constructive discussions and valuable suggestions during the development of this work. This research was supported by the National Science and Technology Council (NSTC) of Taiwan under Grant No. 112-2221-E-194-022-MY3.

Competing interests. The authors declare none

References

1. **Yao S, Liu X, Georgakopoulos SV and Tentzeris MM** (2014) A novel reconfigurable origami spring antenna. In *2014 IEEE Antennas and Propagation Society International Symposium (APSURSI)*, pp. 374–375.
2. **Imran S, Shah H, Gosh S, Tentzeris MM and Lim S** (2018) A novel bio-inspired pattern reconfigurable quasi-Yagi helical antenna using Origami DNA. In *2018 International Symposium on Antennas and Propagation (ISAP)*, pp. 1–2.
3. **Yao S, Liu X and Georgakopoulos SV** (2017) Morphing origami conical spiral antenna based on the Nojima wrap. *IEEE Transactions on Antennas and Propagation* **65**(5), 2222–2232. https://doi.org/10.1109/TAP.2017.2677920.
4. **Shah SIH, Tentzeris MM and Lim S** (2018) A deployable quasi-Yagi monopole antenna using three origami magic spiral cubes. *IEEE Antennas*

https://doi.org/10.1017/S1759078725102821 Published online by Cambridge University Press

and Wireless Propagation Letters **18**(1), 147–151. https://doi.org/10.1109/LAWP.2018.2883380.
5. **Hwang M, Kim G, Kim S and Jeong NS** (2021) Origami-inspired radiation pattern and shape reconfigurable dipole array antenna at C -band for CubeSat applications. *IEEE Transactions on Antennas and Propagation* **69**(5), 2697–2705. https://doi.org/10.1109/TAP.2020.3030908.
6. **Yao S, Bonan Y, Shafiq Y and Georgakopoulos SV** (2018) Rigid origami-based reconfigurable conical spiral antenna. In *2018 IEEE International Symposium on Antennas and Propagation & USNC/URSI National Radio Science Meeting*, pp. 179–180.
7. **Shah SIH, Sarkar A and Lim S** (2020) Electromechanically deployable high-gain pop-up antenna using shape memory alloy and kirigami technology. *IEEE Access* **8**, 225210–225218. https://doi.org/10.1109/ACCESS.2020.3044522.
8. **Rubio AJ, Kaddour A-S, Georgakopoulos SV, Brown N, Ynchausti C and Howell L** (2021) An origami-inspired foldable reflectarray on a straight-major square-twist pattern. In *2021 IEEE 21st Annual Wireless and Microwave Technology Conference (WAMICON), April 2021*, Sand Key, FL, USA.
9. **Kim Y, Phon R, Park E and Lim S** (2023) An additively manufactured deployable broadband metasurface lens antenna. *IEEE Antennas and Wireless Propagation Letters* **22**, 1672–1676. https://doi.org/10.1109/LAWP.2023.3258600
10. **Alkurt FÖ** (2025) Compact horn antenna design based on origami folding process for satellite communication. *Advances in Space Research* **75**(11), 8280–8286. https://doi.org/10.1016/j.asr.2025.03.013.
11. **Chen X, Ge Y, Lin C and Liu X** (2017) Improving the radiation performance of pyramidal horn antennas using a metasurface lens. In *2017 International Applied Computational Electromagnetics Society Symposium (ACES)*, pp. 1–2.
12. **Jiang Z, Zheng P, Qiu Y, Zhu H, Ding C and Wei G** (2020) Mechanically beam-steering of horn antenna using non-uniform flexible meta-surface. In *2020 IEEE 6th International Conference on Computer and Communications (ICCC)*, pp. 463–466.
13. **Lin M-H, Lin -C-C, Lin S-M, Chang -C-C, Lin S-C, Wu J-W and Chang S-F** (2025) Advanced beam reconfiguration in horn antennas through origami-based design. In *2025 19th European Conference on Antennas and Propagation (EuCAP), March 2025*, Stockholm, Sweden.



Chia-Chan Chang (IEEE senior member) received the B.S. degree in Communication Engineering from National Chiao-Tung University, Hsinchu, Taiwan, in 1995, and the M.S. and Ph.D. degrees in Electrical and Computer Engineering from the University of California at Davis, Davis, CA, USA, in 2001 and 2003, respectively. She is now a Professor of Electrical Engineering at National Chung Cheng University, Taiwan. Her research focuses on reconfigurable circuit design, array beamforming, microwave/mm-wave ICs, and innovative radar applications. Prof. Chang has served on the steering committee of the IEEE MTT-S TC-28 and on the technical program review committees of several major international conferences. She was Chair of the IEEE MTT-S Tainan Chapter from 2020 to 2022 and a former Associate Editor of IEEE Sensors Letters. She currently serves as an Associate Editor of IEEE Microwave Magazine.



Chia-Chen Lin received the M.S. degree in Electrical Engineering from National Chung Cheng University, Chiayi, Taiwan, in 2022. He is currently a Hardware Engineer, focusing on chip development and verification, RF hardware design, and hardware implementation for communication systems and satellite payloads. His research interests include RF hardware design, low-Earth-orbit (LEO) satellite communication systems, and antenna and radar design.



Meng-Hsuan Lin (Graduate Student Member, IEEE) received the B.S. degree in Electrical Engineering from I-Shou University, Kaohsiung, Taiwan, in 2017, and the M.S. degree in Electrical Engineering from National Chung Cheng University, Chiayi, Taiwan, in 2019. She is currently pursuing the Ph.D. degree in electrical engineering at National Chung Cheng University. Her research interests include biomedical antenna design, antenna miniaturization, in-body tracking systems, and biomedical radar.



Sheng-Min Lin received the B.S. degree in Electronic Engineering from National Quemoy University, Quemoy, Taiwan, in June 2021, and the M.S. degree in electrical engineering from the National Chung Cheng University, Chiayi, Taiwan, in August 2023. His research focuses on using Origami techniques on Antenna and Lens for Function Enhancement and Meta Horn Design. Since 2023, he has been with Foxconn Industrial Internet Co., Ltd., where he works as a Hardware Development Engineer.



Dengchuan Cai received his Ph.D. in 2001 from the Dept. of Industrial Management of National Taiwan University of Science and Technology, Taiwan. He has over 30 years of teaching experience and is now a professor and Dean of College of Design at NYUST, Taiwan. He possesses a robust enthusiasm for research and innovation in the fields of design science, human factors, mechanical engineering, information technologies, and AI application, with a particular emphasis on assistive technologies, hand tools, vehicle, and furniture design. Prof. Cai received numerous invention patents and innovation awards.

https://doi.org/10.1017/S1759078725102821 Published online by Cambridge University Press